Journal of Building Engineering 79 (2023) 107785

Contents lists available at ScienceDirect

Journal of Building Engineering

journal homepage: www.elsevier.com/locate/jobe

Carbonation of hydrated cement: The impact of carbonation conditions on CO_2 sequestration, phase formation, and reactivity

I.E. Teune *, K. Schollbach, M.V.A. Florea, H.J.H. Brouwers

Department of the Built Environment, Unit Building Physics and Services, Eindhoven University of Technology, P.O. Box 513, 5600 MB, Eindhoven, the Netherlands

ARTICLE INFO

Keywords:
Aqueous carbonation
CO_2 sequestration
Phase mapping
Concrete fines
Pozzolanic reactivity

ABSTRACT

The efficiency of hydrated cement carbonation is often ascribed to the total amount of CO_2 stored by the material. However, the morphology and composition of silicate phases upon carbonation are equally important to unseal the pozzolanic potential of cement recycling for sustainable growth. Therefore, the current study investigates the impact of aqueous- and dry-carbonation (AC and DC) on polymorph formation, silicate microstructure, and porosity of CEM-I as well as CEM–III–derived pastes. The limited diffusion of calcium ions during DC gives rise to the formation of a carbonate shell comprised of calcite, aragonite, and vaterite and results in a 15% lower carbonation efficiency compared to AC. Manual milling was required to expose the amorphous silicate gel and allow for optimal reactivity. AC in 0.1 M sodium hydroxide was found to be the most efficient carbonation method for both reactivity and CO_2 sequestration. Sodium hydroxide allowed for an increased CO_2 capture and thereby promoted rapid carbonation and the formation of a highly porous silicate phase. The presence of sodium hydroxide promotes decalcification but is postulated to limit the pozzolanic reactivity. Although a high calcium content allows for high CO_2 sequestration in CEM-I, for better pozzolanic reactivity a silica-rich material like CEM-III is recommended.

1. Introduction

Human activities in the past two decades have caused an increase in the global surface temperature by 1.1 °C, due to the continued emission of greenhouse gasses [1]. To prevent further damage to the environment, a strong reduction in anthropogenic CO_2 emissions must be achieved. With a production of 4 Gt/year, the cement industry is responsible for approximately 8% of all anthropogenic CO_2 emissions [2]. One way of reducing CO_2 emissions is through carbon capture and utilization, such as the carbonation of cement-rich fines derived from waste concrete [3]. Carbonation of the cement paste stores CO_2 in the form of calcium carbonate and causes the formation of a reactive amorphous silica-alumina gel [4–7]. Using this principle, CO_2 can be used to separate calcium from silica in hydrated cement paste (HCP) and generate pure silica gel [8]. In this process, the carbonation serves two purposes: 1. to store CO_2 and 2. to (re)generate a clean reactive silicate gel. When separated, both products can subsequently be used in a variety of applications such as pigments, pharmaceuticals, or the fabrication of catalytic support materials [9]. Alternatively, carbonated HCP can be used as a supplementary cementitious material (SCM) to lower the clinker content in cement. When mixed with fresh cement, the formed silica gel can react with calcium hydroxide to form a calcium-silica-hydrate (C–S–H) gel which contributes to an increase in compressive

* Corresponding author.
E-mail address: i.e.teune@tue.nl (I.E. Teune).

https://doi.org/10.1016/j.jobe.2023.107785
Received 31 May 2023; Received in revised form 22 August 2023; Accepted 14 September 2023
Available online 15 September 2023

strength [10–12]. Moreover, the addition of calcium carbonate in the form of limestone has been shown to allow for further cement reductions used as a filler, or when mixed with calcined clay [13,14]. The substitution of cement for carbonated HCP, could avoid up to 1.3 Gt of CO_2 emissions and decrease global anthropogenic CO_2 emissions by 2.8% [2,15–17]. Carbonation of HCP, therefore, has the potential to lower CO_2 emissions by storing CO_2 and by reducing the clinker content in cement. To maximize CO_2 reductions, both the reactivity of the silicate gel and the overall CO_2 storage capacity needs to be optimized. Understanding how these two properties are influenced by the carbonation method and material composition is therefore of key importance.

Carbonation can be achieved through dry carbonation (DC) in a climate chamber, or aqueous carbonation (AC) in solution. Multiple studies have focused on understanding and optimizing DC, by varying the carbonation conditions and material composition. It has been shown that conditions such as relative humidity (RH), temperature, and CO_2 concentration impact the speed and degree of carbonation, which subsequently impact properties such as porosity, phase composition, and mineralogy [18,19]. The carbonation efficiency and product formation are further shown to be impacted by material properties such as the Ca/Si (+Al) ratio [20,21], the presence of portlandite [18,22,23], and the presence of other SCMs [24]. In contrast to DC, AC results in fast (~6 h) and complete carbonation of HCP [12,18,25–27]. As with the DC, differences in reaction kinetics are shown to impact the phase composition and morphology of the carbonated material [25,28]. Although the changes in the carbonation method are shown to impact the phase composition and morphology, limited research has been done on the subsequent impact on the pozzolanic reactivity. To unseal the pozzolanic potential of cement recycling for sustainable growth, understanding how the morphology and composition of silicate phases change upon or as a result of carbonation needs to be addressed. To the best of the authors' knowledge, no clear relation between carbonation efficiency and pozzolanic reactivity has been established, nor how carbonation method, and material composition impact this relation.

In this study, the impact of the carbonation method and material composition on CO_2 sequestration and reactivity has been studied. Two types of HCP were subjected to DC and AC in 0.1 M NaOH and water, to investigate the impact of carbonation kinetics on the carbonation efficiency, phase formation, and pozzolanic reactivity [28]. For the HCP, ordinary Portland cement (CEM-I) and a blast furnace slag containing cement (CEM-III) were used, to represent the majority of cement used in the industry [29]. The amount of sequestrated CO_2 and mineralogy was monitored over time to evaluate how the carbonation method, and material composition impact the phase distribution and morphology of the carbonated product. Finally, calorimetric testing was done to investigate how the pozzolanic reactivity is impacted by the material composition and carbonation method.

2. Experimental

Throughout this paper, the following abbreviations and colors are consistently used for the different samples (Table 1).

2.1. Materials and treatments

2.1.1. Hydrated cement pastes

Two different cement pastes were made, following EN 196–3, with a w/b ratio of 0.5 using CEM-I (OPC, 52.5 R, CBR Gent) and CEM-III (70% blast furnace slag, 42.5 N, CBR Gent) respectively [30]. The pastes were cast in 16 × 16 × 4 cm prisms and cured in water for at least 90 days to ensure complete hydration. After curing, the prisms were crushed with a hammer and dried at 40 °C until a steady weight was obtained, after which the material was milled, sieved below 250 μm, and stored in a sealed container until further use.

The oxide composition of the cement pastes was determined with XRF (Epsilon 3, Malvern Panalytical) using the standardless OMNIAN method as shown in Table 2. The materials were prepared by performing loss of ignition (LOI) (12 h at 1000 °C), after which the material is mixed with lithium tetraborate (Claisse borate flux 67.00% $Li_2B_4O_7$ – 33.00% $LiBO_2$, Malvern Panalytical) in a 1:9 ratio and is placed in a borate fluxer oven (Claisse leNeo, Malvern Panalytical) for 29 min at 1065 °C after which the melt is poured into a platinum cast to produce a fused bead. Lithium iodide (5 M, Merck) was used as a non-wetting agent to prevent interference of the $L_{\alpha1}$ line (1.48 keV) of bromine with the $K_{\alpha1}$ line (1.48 keV) of aluminum.

2.1.2. Carbonation

The hydrated cement powders HP-I and HP-III were used for carbonation in a climate chamber (DC-I/III) and aqueous carbonation in water (AC_H-I/III) or 0.1 M sodium hydroxide (AC_{Na}-I/III).

The aqueous carbonation was set up similarly to previous work: a mixture of 15% CO_2 + 85% synthetic air was bubbled through 1.5 l of solution (demineralized water, or 0.1 M NaOH (98.5%, VWR)) as shown in Figure A1 (Appendix A), with a flow of 10 l/h per 1.0 g hydrated cement (EL-FLOW mass flow controller, Bonkhorst, The Netherlands) [27]. After a stable pH was obtained, 150.0 g of hydrated cement powder (1:10 solid:liquid ratio) was added to the solution under continuous stirring. The pH was continuously monitored throughout the carbonation reaction with a Voltcraft PE-03 pH probe (Greisinger GMH 3431, Germany). To study the

Table 1
Sample color reference guide.

Black	HP-I	Powder obtained after sieving and milling hydrated cement paste, made with CEM-I	HP-III	Powder obtained after sieving and milling hydrated cement paste, made with CEM-III
Blue	**AC_{Na}-I**	Carbonated HP-I in 0.1 M NaOH for 6 h	**AC_{Na}-III**	Carbonated HP-III in 0.1 M NaOH for 6 h
Green	**AC_H-I**	Carbonated HP-I in demi water for 6 h	**AC_H-III**	Carbonated HP-III in demi water for 6 h
Red	**DC-I**	Carbonated HP-I in a climate chamber RH 80% and 10% CO_2	**DC-III**	Carbonated HP-III in a climate chamber RH 80% and 10% CO_2

Table 2
Oxide composition of the hydrated cement pastes including the loss of ignition (LOI) after 12 h at 1000 °C.

XRF (wt%)	LOI	CaO	SiO_2	Al_2O_3	MgO	SO_3	Fe_2O_3	Other
HP-I	26.2	50.6	13.1	3.0	0.9	2.7	2.9	0.5
HP-III	24.5	40.2	21.0	5.0	4.4	2.9	0.9	1.1

carbonation progress, various samples of the suspension were taken at specific changes in pH. The samples were filtered (filter paper <2 μm VWR), washed with an excess of isopropanol (VWR, technical grade >98%), diethyl ether (VWR, 99%), and dried under a vacuum to stop hydration. The samples were subsequently stored in a sealed container until further analysis was carried out. The carbonation was stopped after a stable pH was obtained for 1 h (around 5–6 h of carbonation depending on the material).

Dry carbonation (DC) of the hydrated cement pastes was done in a climate chamber (Airtemp, Germany) at 10% CO_2, 20 °C, and relative humidity of 80%. 10 × 10 g of HCP was evenly distributed in a Petri dish to sure optimal exposure. The material was stored for a total of 28 days to ensure complete carbonation, although complete carbonation was already observed after 7 days as confirmed with Q-XRD and TGA. The carbonation process was stopped by washing the samples in isopropanol and diethyl ether as described above.

2.2. Characterization methods

2.2.1. SEM–EDX

SEM-EDX measurements for PARC analysis were done on embedded samples with a JEOL JSM-7001F 33 mm^2 (Thermo Fischer Scientific) equipped with SSD detectors and EDX NORAN System 7 hardware with NSS 3.3 software using 15 kV voltage, 6.2 nA beam current, and a step size of 1 μm. The material was embedded in epoxy resin (Stuers EpoFix) and subsequently polished without water and coated with carbon. The obtained images were analyzed with the PhAse Recognition and Characterization (PARC) software [31]. The grains are automatically detected and the surrounding empty embedding material is excluded. The detected grains were then automatically sorted by size and stitched together into one large SI-file. Eight different phases were distinguished based on the EDX data and the pixels were grouped accordingly. A density plot was further used to divide the PARC group into calcium hydroxide and carbonate instead [31]. The carbonated samples do not contain calcium hydroxide as seen with Q-XRD and therefore no density plot was used there. SEM analysis of the morphology is carried out on a Phenom ProX (Thermo Fischer Scientific), equipped with a backscattering electron detector with a spot size of 4.0 and 15 kV voltage. The material was sprinkled on a carbon stub and coated with a 14-nm gold layer (K575x Dual Turbo sputter coater).

2.2.2. N_2–physisorption

Measurements were carried out on a Tristar II 3020 V1.03 (Micromeritics). The materials were degassed by heating them to 120 °C under a continuous nitrogen flow.

2.2.3. Laser granulometry

Particle size analysis was carried out on a Mastersizer2000 (Malvern) by dispersing the materials in isopropanol to minimize agglomeration and prevent further reaction. The distribution was averaged over three measurements and conducted at different stirring speeds to ensure proper dispersion.

2.2.4. Quantitative XRD

Before analysis, the materials were mixed with 10 wt% Si as an internal standard and milled for 15 min with an XRD mill (McCrone, Retsch, Germany) for homogenization. The measurements were conducted with a Bruker D4 (Co tube, $K_{\alpha1}$ 1.7901 [Å] $K_{\alpha2}$ 1.7929 [Å], step size 0.018 2Theta, range 10–90 2Theta) with an LYNXEYE 1-D detector and fixed divergence slits with an opening of 0.5° and 0.03 rad soller slits. The phases were identified with X'Pert HighScore Plus 2.2. (PANalytical) using the ICDD PDF-2 database. For the quantification of the mineral phases in the samples, the TOPAS software version 4.2 from Bruker was used.

2.2.5. Thermogravimetric analysis

TGA was carried out on an STA 449 F1 Jupiter (Netzsch) equipped with Pt crucibles under a nitrogen atmosphere (20 ml/min) and a heating ramp of 10 °C/min from 40 to 1040 °C [32]. For quantification of the carbonate content, slight variations in temperature ranges were tested to make sure the error of quantified amounts would fall below 5% or 0.1 wt%.

2.2.6. Infrared spectroscopy

ATR-IR analysis was done with a Frontier FTIR (PerkinElmer) equipped with diffuse reflectance device GladiATR. The spectra were averaged over 10 scans in a range from 4000–400 cm^{-1} with a 1 cm^{-1} resolution. The samples were measured both before and after milling.

2.2.7. Calorimetry

The reactivity of the carbonated materials was studied with isothermal calorimetry (TAM Air, Thermometric 3-channel) using the R^3 method described in the work of Scrivener et al. [33]. In a 15 ml vial, 1.00 g of sample was mixed with 3.00 g of $Ca(OH)_2$. (Acros organics, 98%, extra pure). Subsequently, 4.8 ml of 0.094 M KOH (VWR, 86.7%) 0.14 M K_2SO_4 (Sigma-Aldrich >99%) is added to the material after which the mixture was mixed with a vortex mixer for 30 s, lowered into position and measured. Before inserting the samples, a baseline was measured for 1 h with a maximum variation of 0.01 mW. After insertion, the first 45 min were not taken into account to minimize errors in the heat measured which are introduced upon insertion and mixing [32]. After 140 h, the samples were

removed from the calorimeter. The hydration was stopped as described in Paragraph 2.1.2, by washing with isopropanol, and diethyl ether and subsequently drying in a vacuum oven and storing in a sealed container until further analysis.

3. Results and discussion

The analysis of the materials before and after carbonation is split into six paragraphs. First, the carbonation degree and degree of decalcification are studied using TGA (Paragraph 3.1), after which the difference in carbonation mechanism is studied in more detail with Q- XRD and in-situ pH (Paragraphs 3.2 and 3.3). Next, the chemical composition is studied in more detail with PARC and FT-IR analysis (Paragraph 3.4), followed by characterization of the morphology with SEM, BET, and laser granulometry (Paragraph 3.5). Finally, the reactivity is determined with calorimetry and TGA (Paragraph 3.6).

3.1. Carbonation degree

To determine the total amount of CO_2 sequestrated by the carbonated CEM-I and CEM-III samples, thermogravimetric analysis (TGA) was carried out, as shown in Fig. 1 and Table 3.

The amounts of $Ca(OH)_2$ and $CaCO_3$ are determined by:

$$\%\ Ca(OH)_2 = \frac{\Delta M\ Ca(OH)_2}{\frac{Mm_{H_2O}}{Mm_{Ca(OH)_2}}} \cdot \frac{M^{HP}_{1000°C}}{M_{1000°C}} \tag{1}$$

$$\%\ CaCO_3 = \frac{\Delta M\ CaCO_3}{\frac{Mm_{CO_2}}{Mm_{CaCO_3}}} \cdot \frac{M^{HP}_{1000°C}}{M_{1000°C}} \tag{2}$$

Where Mm is the molar mass in g/mol, ΔM is the change in weight in wt%, and $M^{HP}_{1000°C}$ is the wt% of the HPs at 1000 °C to account for the weight increase during carbonation. As shown in Fig. 1, the DC materials show a gradual weight loss between 460 °C and 820 °C due to the decomposition of amorphous carbonates (400–600 °C), and calcium carbonate polymorphs such as aragonite and vaterite (530–650 °C) and calcite (650–850 °C), which is further confirmed with XRD (Figure B1, Appendix B) [18,32,34,35].

Quantitative X-ray diffraction (Q-XRD) was done on the same samples, to complement the TGA results (Table B1 and B2, Appendix B). The weight increase during the carbonation is accounted for by normalizing the mineral phase composition according to the mass of the HPs at 1000 °C as determined with TGA.

As shown in Table 3, the total $CaCO_3$ content of the carbonated samples determined with TGA is in good agreement with the Q-XRD results, with less than a 5% difference in the total quantified amount. The HP samples have an overall lower amount of $CaCO_3$ (~60%) and $Ca(OH)_2$ (~20%) compared to the quantities determined with TGA, which can be due to the presence of amorphous or poorly crystalline phases which are XRD invisible [26]. The reduced amount of $Ca(OH)_2$ in HP-III (2.7–3.4 wt%) is due to the lower clinker content, and the pozzolanic reaction of amorphous silicates in the blast furnace slag in CEM-III [36]. For further calculations, the quantification with TGA was used as it accounts for the poorly crystalline phases.

To estimate the efficiency of the carbonation method, the carbonation degree (i.e. % of calcium which is carbonated) was calculated (Table 4):

$$Carbonated\ Ca\ (\%) = \frac{M\ CaCO_3\ sample}{M\ CaCO_3\ calculated} \cdot 100\% \tag{3}$$

$$M\ CaCO_3\ calculated = \frac{M\ CaO^{HP} \cdot Mm\ CaCO_3}{Mm\ CaO} \tag{4}$$

Where M $CaCO_3$ is the amount of calcium carbonate in wt% as determined with TGA (Table 3), Mm is the molar mass (g/mol), and M CaO^{HP} is the amount of CaO in hydrated cement paste as determined with XRF (Paragraph 2.1, Table 2). The carbonation degree is

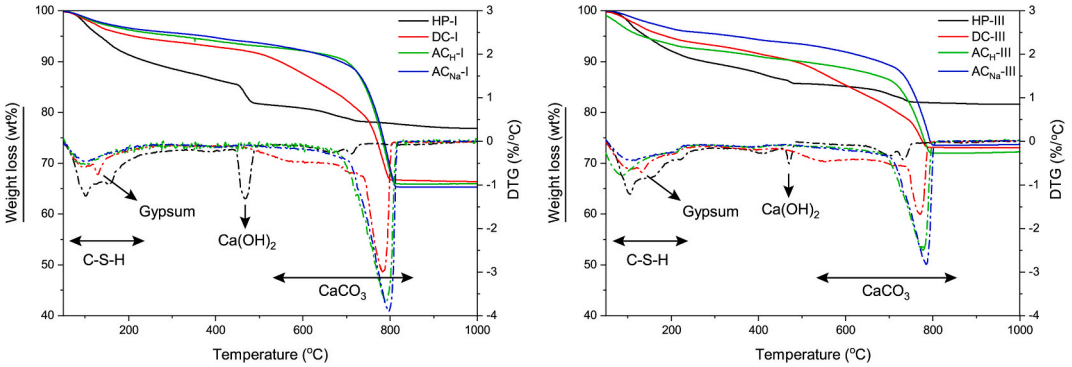

Fig. 1. TG (solid line)-DTG (dotted line) data of the CEM-I derived samples (left) and CEM-III derived samples (right).

Table 3
Chemical composition based on TGA and Q-XRD quantification.

	HP-I	AC_H-I	AC_{Na}-I	DC-I	HP-III	AC_H-III	AC_{Na}-III	DC-III
Q-XRD (wt%)								
Portlandite	13.9	0.0	0.0	0.4	2.7	0.0	0.0	0.0
Calcite	2.5	73.8	75.7	28.6	3.7	48.9	50.0	19.4
Vaterite	0.0	0.0	0.0	21.8	0.0	0.0	0.0	15.9
Aragonite	0.0	0.0	0.0	14.0	0.0	0.0	0.0	7.0
Total $CaCO_3$	2.5	73.8	75.7	64.4	3.7	48.9	50.0	42.2
TGA (wt%)								
$Ca(OH)_2$	17.3	0.0	0.0	0.6	3.4	0.0	0.0	0.0
$CaCO_3$	7.3	72.0	76.6	67.8	9.3	46.4	50.5	40.0

Table 4
Calculated carbonation degree and Ca/Si ratio after carbonation.

	HP-I	AC_H-I	AC_{Na}-I	DC-I	HP-III	AC_H-III	AC_{Na}-III	DC-III
% Ca carbonated	11	80	85	75	13	65	70	56
Ca/Si		0.77	0.57	0.96		0.67	0.57	0.84

defined as the percentage of calcium that is successfully carbonated and is not corrected for the presence of magnesium due to the absence of any dolomite, or magnesium carbonate species, in the XRD diffractograms. Since the carbonation degree is normalized to the total amount of calcium in the material, the same carbonate content can lead to different carbonation degrees. A side-by-side comparison of CEM-I and CEM-III can therefore be misleading and does not reflect the efficacy with which calcium is removed from the calcium silicate hydrate (C–S–H) gel. At Ca/Si ratios below 0.67, all interlayer calcium has been removed from the C–S–H gel and residual calcium ions reside in the main layer, sandwiched by potentially infinite chains of silica tetrahedrons making it harder to carbonate [18,21–23]. The Ca/Si ratio, therefore, provides a better indication of the decalcification efficiency, and thereby of the efficiency of the carbonation. Using the carbonation degree, an estimation of the Ca/Si ratio of the decalcified C–S–H gel can be made:

$$\frac{Ca}{Si} = \frac{(1 - \%\ carbonated\ Ca) \cdot \left(M\ CaO^{HP}\right)}{M\ SiO_2^{HP}} \tag{5}$$

Where M CaO^{HP} and M SiO_2^{HP} is the mass fraction of CaO and SiO_2 in hydrated cement paste as determined with XRF (Paragraph 2.1, Table 2). The calculated Ca/Si ratio does not account for the presence of other calcium- or silica-containing phases, since only negligible (~2 wt%) amounts were identified by Q-XRD after carbonation (Table B1, Appendix B).

As shown in Table 4, the final Ca/Si ratio of AC_{Na}-I and AC_{Na}-III is 0.57, whereas their carbonation degrees are 85% and 70%

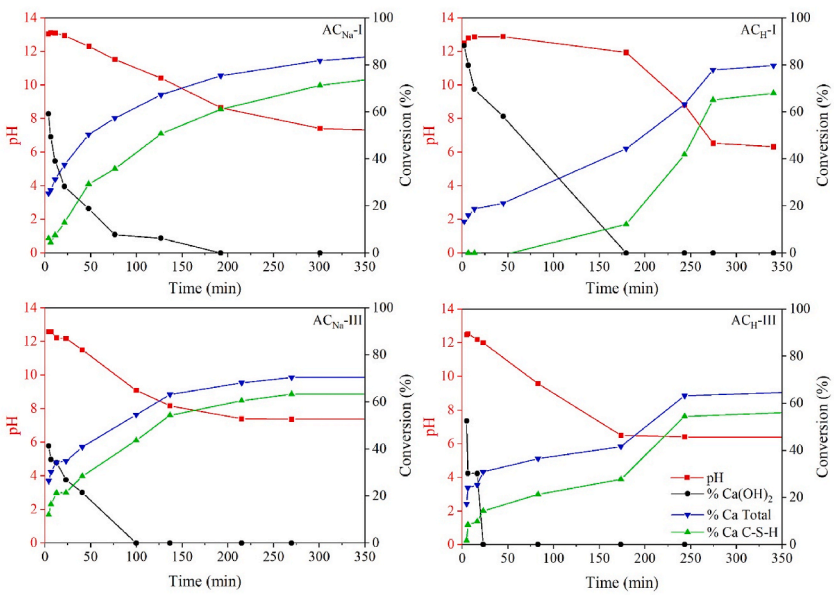

Fig. 2. pH, $Ca(OH)_2$ conversion, total carbonation degree, and % of carbonation from C–S–H over time. Top: CEM-I derived samples in 0.1 M NaOH (left) and water (right). Bottom: CEM-III derived samples in 0.1 M NaOH (left) and water (right).

respectively. Using the Ca/Si ratio can therefore provide a better indicator of the carbonation efficiency, where carbonation efficiency is defined as the ability of a method of material to decalcify the C–S–H. An overall improved carbonation efficiency can be attributed to the CEM-III samples as reflected by the lower Ca/Si ratios (~0.57–0.84). The lower calcium content of the CEM-III (40.2 wt%) could lead to earlier decalcification of the interlayer calcium leading to lower Ca/Si ratios. Overall, the highest carbonation efficiency is achieved for carbonation in 0.1 M NaOH (85% and 70%) and is lowest for the dry carbonated samples (75% and 56%), irrespective of the cement used.

3.2. Aqueous carbonation over time

To better understand how the carbonated material is affected by the carbonation method, the carbonation progress over time was studied. To differentiate between the carbonation of $Ca(OH)_2$ and of the C–S–H gel, the carbonation degree of the C–S–H gel was estimated by Equation (7). Here, the change in mol $Ca(OH)_2$ was subtracted from the respective increase in mol $CaCO_3$ and summed up over the different time intervals. The amount in moles is calculated by dividing the quantity as determined with TGA (Table C1, and C2, Appendix C) by the molar mass of the respective phase.

$$Conversion\ Ca(OH)_2\ (\%) = \frac{M\ Ca(OH)_2{}^{t^i}}{M\ Ca(OH)_2{}^{HP}} \bullet 100\% \tag{6}$$

$$mol\ Ca_{C-S-H}^{HP} = mol\ CaO_{XRF}^{HP} - mol\ CaCO_3{}^{HP} - mol\ Ca(OH)_2{}^{HP} \tag{7}$$

$$Conversion\ Ca_{C-S-H}\ (\%) = \sum_{t=0}^{t^i} \frac{\Delta[mol\ CaCO_3]_{t^{i-1}}^{t^i} - \Delta\left[mol\ Ca(OH)_2\right]_{t^{i-1}}^{t^i}}{mol\ Ca_{C-S-H}^{HP}} \bullet 100\% \tag{8}$$

As shown in Fig. 2, the NaOH samples show a high initial carbonation (37-35%) within the first 20 min, followed by a slow continuation of the carbonation whereas the H_2O samples have a lower carbonation degree (20–30%) and show a rapid increase in carbonation after 170 min.

The high initial carbonation of the NaOH samples can be ascribed to the increased concentration of CO_2 caused by the sodium ions and the initial high pH of the system [27,37]. These conditions have been reported to result in high undersaturation (i.e. fast dissolution) of hydration phases such as portlandite, in contrast to the H_2O system [25,26,28]. After the portlandite is consumed in the NaOH samples, and the pH starts to drop, carbonation is primarily dominated by the dissolution of the hydration phases which are limited by the presence of alkali [26,28].

The decrease in carbonation speed is hypothesized to be due to the inclusion of sodium which hinders further decalcification by acting as a diffusion barrier. SEM/EDX analysis (Table D1, Appendix D) further confirms an increased sodium content (3.6 wt%) in the silicate gel phase. It is known that sodium can substitute calcium in the C–S–H gel, and could thus promote the decalcification of the C–S–H [38]. It can therefore be envisioned that sodium initially enables fast carbonation by acting as a charge-compensating ion during the initial carbonation phase. This is further supported by the work of Bernard et al., where it was shown that a low Ca/Si ratio at high pH results in a higher alkali binding capacity [38,39]. For the NaOH samples, the rapid decalcification leads to the formation of a negatively charged, silica-rich surface of the C–S–H particle which is then stabilized by sodium (Equations (9) and (10)).

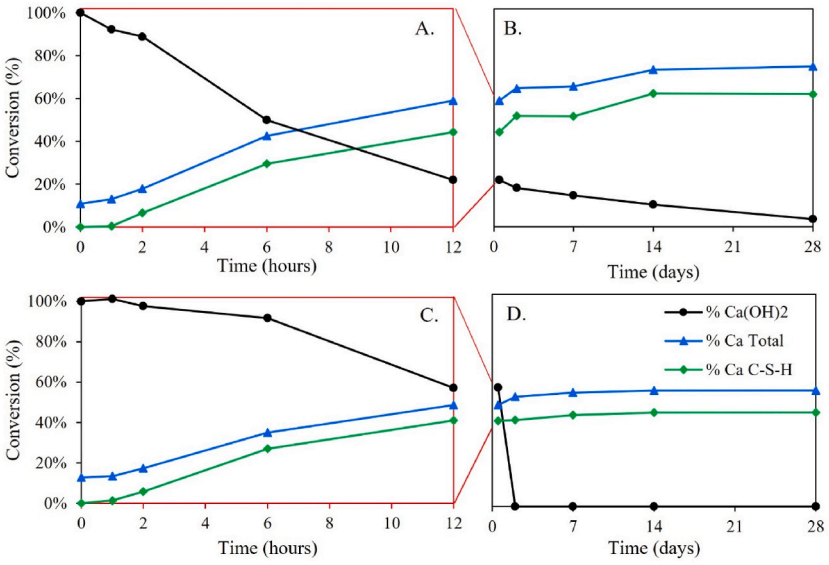

Fig. 3. Comparison of $Ca(OH)_2$ conversion, total carbonation degree, and % of carbonation from C–S–H. Top: CEM-I-derived samples (A, B). Bottom: CEM–III–derived samples (C, D).

$$Ca_xSiO_z\ (s) + H_2O\ (l) \leftrightarrow xCa^{2+}\ (aq) + [SiO_z]^{2x-}\ (s) \quad (9)$$

$$[SiO_z]^2(s) + H_2O\ (l) \leftrightarrow [SiO_{z\text{-}1}\ \text{–OH}]^{2x-\ +1}\ (s) + OH^-\ (aq) \quad (10)$$

However, after the rapid initial decalcification (~10–20 min), the sodium can act as a diffusion barrier, thereby slowing down the dissolution of calcium and its carbonation.

The solubility of the hydration phases in the H_2O system is primarily pH dependent and not limited by the presence of alkali, thus resulting in a steep increase in carbonation after all the portlandite is carbonated and the pH starts to drop (~170 min). During this phase, the nucleation of calcium carbonates dominates as opposed to the growth of existing calcite in the H_2O system, which is further supported by the small crystal formation (Fig. 8) [25,26,28].

3.3. Dry carbonation over time

To compare the carbonation of the AC samples to the DC samples, the total carbonation (Equation (3)), converted $Ca(OH)_2$ (Equation (6)), and carbonation of the C–S–H (Equation (8)) were calculated for the DC samples (Fig. 3). The Q-XRD and TGA quantification can be found in Appendix B and C respectively.

Since carbonation in the climate chamber resulted in the formation of different calcium polymorphs, the total carbonate content was compared to the calcium carbonate polymorph composition at selected times (Fig. 4, Table B1 and B2, Appendix B). For the DC samples, the carbonation can only occur in the water adsorbed on the surface of the material. The carbonates will therefore precipitate on the surface and result in the formation of a carbonate layer around the particles. As shown in Fig. 3, both the total carbonation and carbonation of the C–S–H increase most between 2 and 6 h and at an approximately equal rate, indicating simultaneous carbonation of the C–S–H gel and the portlandite. Moreover, it can be observed that ~50–60% of the carbonation occurs in the first 12 h, after which the carbonation significantly slows down and levels of around 56–75%.

As shown in Fig. 4, the main carbonation products at 6 h are vaterite and calcite, where the formation of vaterite dominates in both samples (22 wt% and 14 wt%) [19]. During the first 2 h, the total carbonate content as determined with TGA is higher than the XRD quantified amount, indicating the formation of amorphous calcium carbonate, which can transform to form vaterite at later ages [40]. Indeed at 14 days, the formation of aragonite is observed. The formation of aragonite is also associated with lower Ca/Si ratios as well as reduced RH [18]. The formation of the aragonite after 14 days could therefore be indicative of limited dissolution of calcium ions. No change in composition or carbonate content is observed after 14 days, showing that the carbonated material is stable. The lowered carbonation degree of the DC samples is therefore assumed to be due to diffusion limitations caused by the carbonate layer around the particles and the low RH [18,19].

3.4. Phase composition

To further study the amorphous phase composition, SEM/EDX analysis was performed on the CEM-I samples (Fig. 5). The data were analyzed with PhAse Recognition and Characterization (PARC) software to generate phase maps, providing an area% of each phase and its average chemical composition (Table D1, Figure D1. Appendix D) [31].

From Fig. 5, a clear change in the composition of phases can be observed after carbonation, where most C–S–H and $Ca(OH)_2$ have transformed into calcium carbonate, Si-rich C–S–H, and silica. The DC particles contain a thick calcium carbonate layer at the rim of the particles and appear to have a decreasing calcium gradient moving from the rim to the center of the particles where a silica-rich is formed. It can be observed that voids appear to be located inside these silica phases both in the DC and AC samples. The formation of silica gel upon decalcification requires polymerization and restructuring of the C–S–H gel, causing shrinkage and thereby creating voids in the material [23,41]. The formation of the silica phase is most prominent in the AC samples, which contain approximately 18–21 wt% silica phase in contrast to 2 wt% in the DC. The high silica content appears to be associated with an increased formation of voids and cracks and appears to be highest for the AC_H-I sample. Moreover, the silicate phase appears to be more homogeneous compared to the AC_{Na}-I sample (Figure D2, Appendix D). This could be related to the difference in reaction kinetics, where the slower carbonation of the AC_H sample results in a more gradual decalcification of the silicate gel, allowing for a more homogeneous distribution of the calcium throughout the gel.

To further study the composition of the carbonated materials, FT-IR analysis was carried out on the materials [42,43]. To expose

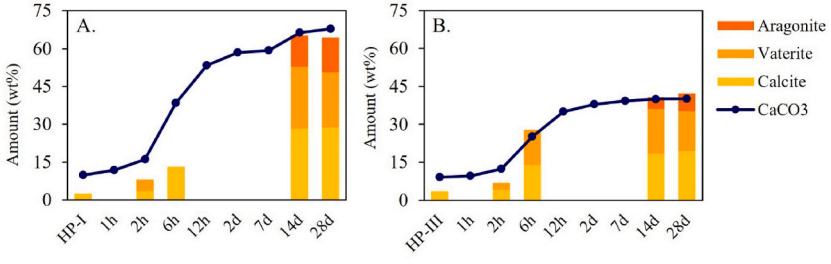

Fig. 4. Total amount of $CaCO_3$ as determined with TGA compared to the carbonate composition as determined with Q-XRD. A. CEM-I-derived samples, B. CEM–III–derived samples.

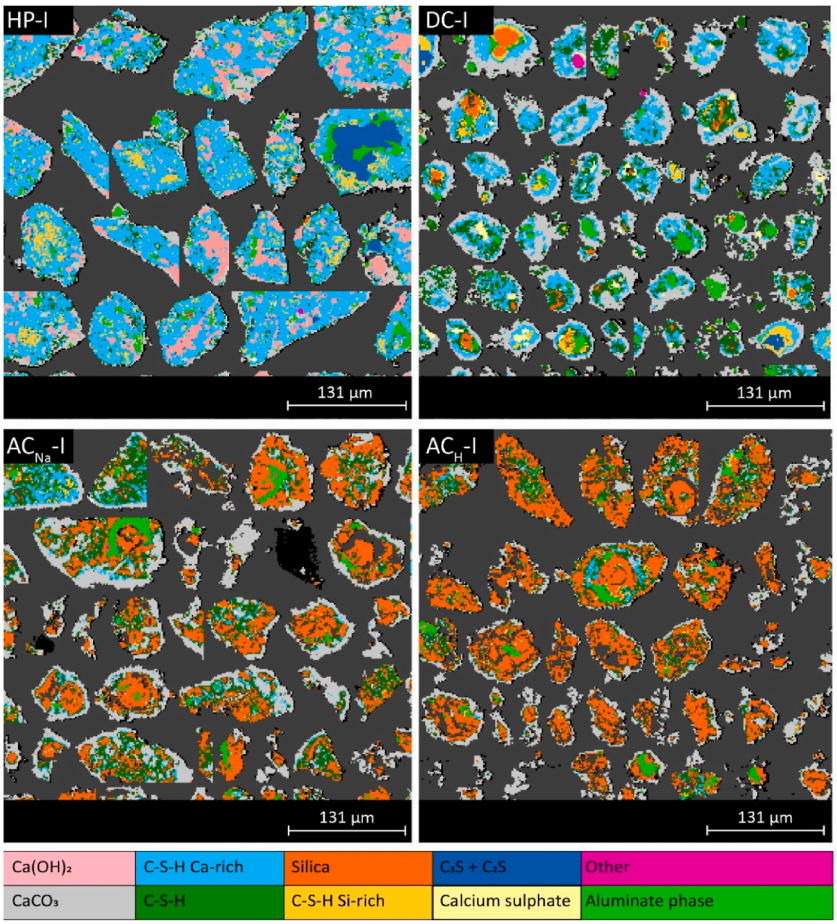

Fig. 5. Phase map of the CEM-I derived materials before and after carbonation using PARC.

the phases, present at the center of the materials, the material was measured both before and after milling. As Fig. 6 shows, milling of the material changes the ratio of the different bands due to exposure of the phases inside the material. Generally, it can be assumed that the area of a band and the intensity ratio of different bands correlate well with the relative amount present in the sample [44,45].

The localization of the silica-rich phase at the center of the carbonated materials was additionally confirmed by the increased intensity of the Si–O bending vibration at 1030 cm^{-1} after milling the material [44–46]. This was accompanied by a slight shift of approximately 4–6 cm^{-1} to higher wavenumbers, indicating increased polymerization of the silicates inside the material [28]. No significant changes in band position were observed upon comparing the CEM-I and CEM–III–derived samples, indicating a similar degree of polymerization.

The sharp bands around 875-855 cm^{-1} can be attributed to different calcium carbonate polymorphs (Table E1, Appendix E), where aragonite has a unique sharp band at 854 cm^{-1} and vaterite and calcite have a combined vibrational band around 874 cm^{-1} [42,43]. The presence of a band at 854 cm^{-1} in the spectra of DC-I and DC-III confirms the presence of aragonite in these samples as shown with XRD (Figure B1, Appendix B). After milling, the intensity of this band is reduced compared to the band at 874 cm^{-1} which indicates that the aragonite is primarily located on the outer surface of the particles.

The band at 1130 cm^{-1} can be ascribed to the sulfate asymmetric $\nu 3$ vibration [42]. The presence of this band in the DC samples can be ascribed to the reformation of gypsum, as is further confirmed by Q-XRD (Table B1, and B2, Appendix B). Before milling, the AC_H samples also contain a band at 1130 cm^{-1}, suggesting some residual sulfates on the surface. This is further confirmed by the increased sulfate concentration in the Ca-rich C–S–H (4.2 wt%) according to PARC analysis (Table D1, Appendix D).

3.5. Porosity generated due to carbonation

As shown in Fig. 5, the carbonated materials appear to have an increased porosity which can affect the reactivity when used as a supplementary cementitious material (SCM). An increased reactivity has been associated with an increased specific surface area (SSA) and is, therefore, an important factor impacting the pozzolanic reactivity of the carbonated material [47–50]. Therefore, the morphological changes after carbonation were studied.

As shown in Fig. 7, both CEM-I and CEM-III materials show similar changes in particle size distribution (PSD) after carbonation. After AC, a narrower distribution is obtained which is shifted towards a smaller particle size with a d_{50} value ~20–40% lower than the

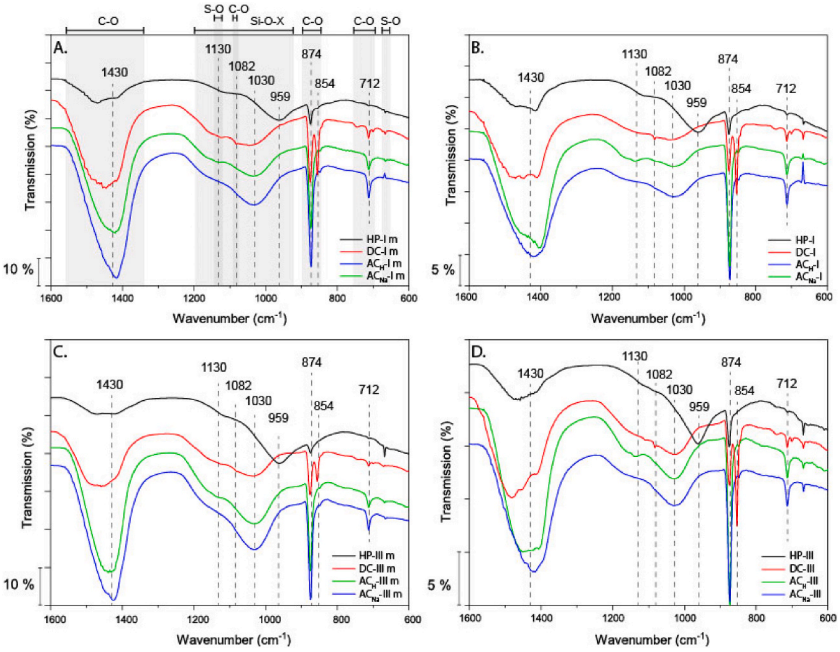

Fig. 6. FT-IR spectra of the CEM-I-derived samples with and without milling (A, and B.) and CEM–III–derived samples with and without milling (C. and D.). The C–O vibrations, Si–O vibrations, and S–O vibrations are highlighted in blue, yellow, and red respectively. (For interpretation of the references to color in this figure legend, the reader is referred to the Web version of this article.)

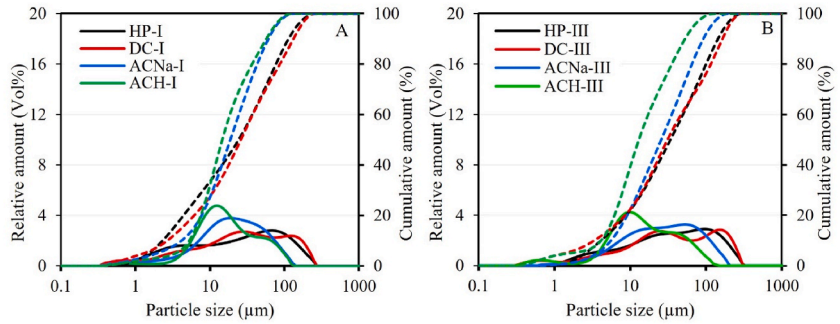

Fig. 7. Cumulative (dotted line) and relative (solid line) PSD of CEM-I derived samples (A.) and CEM-III derived samples (B) before and after carbonation treatments.

initial starting material (Table 5). The reduction in d_{50} and narrowing of the PSD is possibly caused by the dissolution of the calcium from the HCP particles and the subsequent growth of calcite crystals in the solution and on the surface of the HCP. A stronger reduction in size is observed for the AC_H samples (~40–60%), which is related to the slow initial reaction allowing for more dissolution, and precipitation of smaller calcite crystals [26,28,51]. This is further confirmed with SEM (Fig. 8). After DC, the whole PDS shifts towards a higher particle size, which is due to the precipitation of the calcium carbonate on the surface of the particles.

The percentual change in size, surface area, and pore volume is calculated compared to the original hydrated cement paste and indicated in the square brackets.

As shown in Table 5, the change in d_{50} of the CEM-III materials is comparable to the CEM-I materials. The total surface area and pore volume are higher for the CEM-III samples, although the relative change in pore volume and surface area is slightly higher in the CEM-I samples. The increase in pore volume is related to the amount of decalcification of the C–S–H, where the removal of more calcium ions results in more shrinkage of the C–S–H [12,22,23]. Overall, the trend in SSA and porosity is similar for both materials and depends primarily on the carbonation method, where carbonation in NaOH creates the most porous material, and dry carbonation has the highest surface area. In line with the higher carbonation degree (Table 3), the AC samples have a higher porosity compared to the DC. As shown in Fig. 8, SEM analysis of the particles shows the formation of needle-like crystals in the DC samples, which can be ascribed to the presence of aragonite [34,52]. The high SSA of the DC samples is therefore not only caused by the shrinkage of the C–S–H gel but also by the formation of needle-like aragonite. The surface of the AC-treated materials is primarily covered by stout-shaped crystals where the AC_H samples have smaller crystals covering the surface compared to the AC_{Na} samples [26,28]. This explains the increased average particle size of the AC_{Na} samples (d_{50} ~28 μm) compared to the AC_H samples (d_{50} ~14–16 μm).

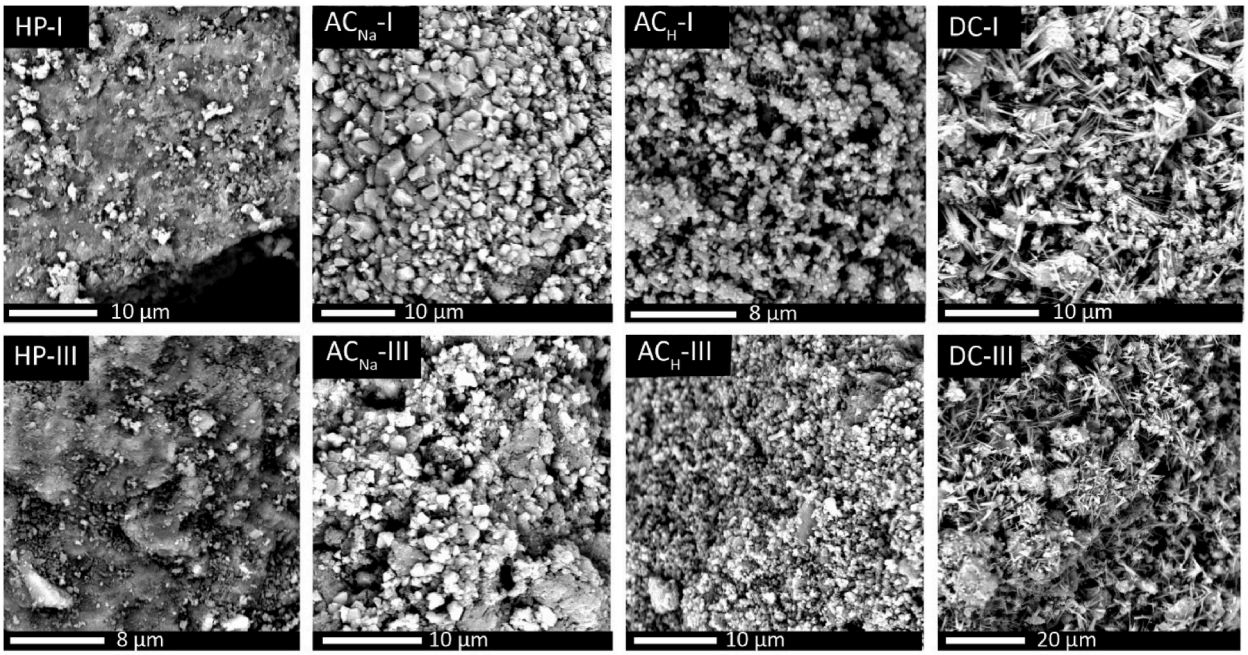

Fig. 8. SEM images of the materials before and after carbonation.

Table 5
d_{10}, d_{50}, and d_{90} values and BET and BJH pore volume of the hydrated cement pastes (HP) before and after dry- and aqueous carbonation treatments.

Sample	d_{10} (µm)	d_{50} (µm)	d_{90} (µm)	BET surface area (m^2/g)	BJH pore volume (1.7–300 nm) (cm^3/g)
HP-I	2.6	27.1	125.0	11.6	0.07
DC-I	2.9 [+11%]	28.6 [+6%]	145.8 [+17%]	63.9 [+452%]	0.13 [+86%]
AC_{Na}-I	4.6 [+77%]	20.8 [-23%]	67.4 [-46%]	48.1 [+316%]	0.14 [+100%]
AC_{H}-I	5.8 [+123%]	16.2 [-40%]	63.3 [-49%]	50.9 [+340%]	0.13 [+86%]
HP-III	4.5	37.5	158.8	18.3	0.12
DC-III	3.6 [-20%]	33.9 [-10%]	180.7 [+14%]	91.6 [+401%]	0.14 [+17%]
AC_{Na}-III	6.2 [+38%]	28.4 [-24%]	101.6 [-36%]	54.0 [+195%]	0.21 [+75%]
AC_{H}-III	4.5 [+0%]	14.1 [-62%]	57.0 [-64%]	74.9 [+309%]	0.20 [+67%]

3.6. Effect of carbonation on pozzolanic reactivity

To further study the effectiveness of the carbonation in terms of reactivity regeneration, the pozzolanic reactivity of the carbonated materials was measured using the R^3 test [33].

In Fig. 9 both the continuous and cumulative heat release is plotted for the carbonated CEM-I and CEM–III–based materials. The DC sample was tested before and after manually grinding the material in a mortar and pestle to expose the silica phase (Fig. 5). Grinding increased the heat release by 37 J/g and 19 J/g respectively, which suggests that the carbonate layer is indeed hindering the reaction of the silicate phase. The AC samples display a high initial heat flow within the first 40 h, which can be related to the increased porosity of these samples which allows for a faster reaction. Overall, a higher heat release is observed in the CEM–III–derived samples compared to the CEM-I-derived samples due to the overall higher silica content in the blast furnace slag. This is in contrast with the carbonation degree and the total amount of carbonated calcium (Table 3), which is higher for the CEM-I samples.

To better understand this, the available amorphous silica content was estimated. Based on the C–S–H carbonation degree (Equation (8)) and total silica content (XRF, Table 2), an estimation can be made of the available amount of amorphous silica (Equation (11)).

$$SiO_2^{available} = SiO_2^{XRF} \bullet \%\ Ca\ C-S-H_{carbonated} \tag{11}$$

Theoretically, the silica should be able to react with calcium hydroxide to reform the C–S–H gel. Therefore, the consumed amount of calcium hydroxide was calculated, based on TGA (Table F1, Appendix F):

$$Ca(OH)_2^{reacted} = \left(M\ Ca(OH)_2^{initial} - M\ Ca(OH)_2^{final} \bullet \frac{M_{initial}^{1000°C}}{M_{final}^{1000°C}} \right) - \left(M\ CaCO_3^{final} \bullet \frac{M_{initial}^{1000°C}}{M_{final}^{1000°C}} - M\ CaO_3^{initial} \right) \tag{12}$$

The amount was corrected for the amount of $Ca(OH)_2$ and $CaCO_3$ before the reaction and normalized to account for the weight increase due to the carbonation. $M_{initial}^{1000°C}/M_{final}^{1000°C}$ is the normalization factor where $M_{initial}^{1000°C}$ is the theoretical weight of the sample at

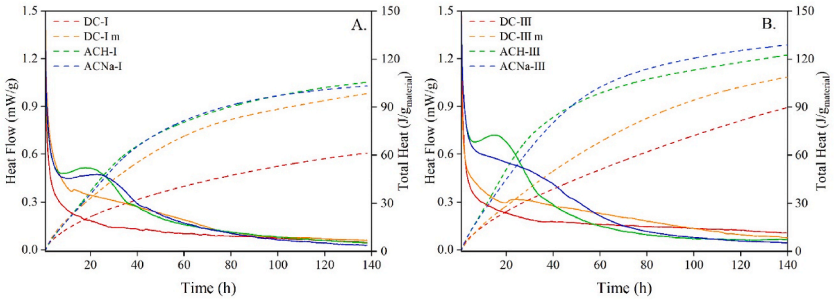

Fig. 9. Heat flow (solid line) and total heat (dotted line) of the materials in the R^3 calorimetry measurement after 45 min of reaction. A. CEM-I-derived samples B. CEM–III–derived samples.

1000 °C and $M_{final}^{1000°C}$ is the actual weight of the sample at 1000 °C in wt%.

As shown in Fig. 10, the calcium consumption increases for the DC samples after grinding the material, thereby confirming that the reactivity of the silicate phase is hindered by the carbonates covering the surface of the material. The trend in total heat release appears to follow a similar trend as the silicate content. Although the quantification of the consumed $Ca(OH)_2$ roughly follows the same trend as the total heat release, partial carbonation of the residual $Ca(OH)_2$ could not be avoided during sample preparation and measurement, which made it difficult to correctly quantify the amount of consumed portlandite due to rescaling. The trend in consumed $Ca(OH)_2$, therefore, seems less in line with the total heat release. The same has been observed for pure silicate systems, where the total heat release is shown to be dependent on the Ca/Si ratio of the reagent [47]. Based on these results, the available silicate content appears to be a better indicator of the potential reactivity of the carbonated material, if exposed properly.

The silicate content and heat release align well for the DC and AC_H samples, but the heat release of the AC_{Na} samples appears to be lower than expected based on the silica content. As shown in Fig. 5, the particles are surrounded by a slightly thicker layer of carbonates compared to the AC_H samples. Like the DC samples, the decreased reactivity might be due to the carbonates hindering the reactivity of the silicates. However, the high porosity (Table 5) makes this a less likely explanation. It can be hypothesized that the increased sodium content hinders the pozzolanic reactivity, by limiting the uptake of calcium to reform the C–S–H gel. However, more work is needed to confirm this.

Overall, these results indicate that the carbonated materials can be used as effective SCMs where silica-rich materials, like CEM-III, appear to be more reactive compared to calcium-rich materials like CEM-I. Aqueous carbonation results in the highest reactivity, but further research is required to understand how the pozzolanic reactivity is affected by the inclusion of other elements and porosity.

4. Conclusions

In the presented work, the CO_2 sequestration efficiency and pozzolanic reactivity are investigated in relation to the material composition and carbonation method. In this work, three definitions of carbonation efficiency are used to showcase that carbonation 'efficiency' can be interpreted in different ways depending on the goal and application.

1. The carbonation degree (% of calcium carbonated), i.e. the ability of a material to store CO_2.
2. The degree of decalcification, i.e. ability to remove calcium from the C–S–H gel as reflected by the Ca/Si ratio.

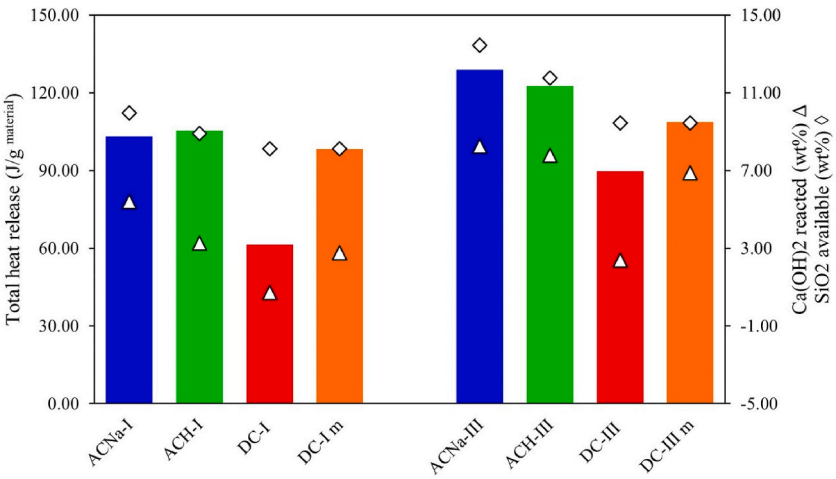

Fig. 10. Total heat release versus the amount of consumed $Ca(OH)_2$, and available amount of SiO_2.

3. The total heat release, which reflects the pozzolanic reactivity of a material in the R^3 test.

The carbonation degree was shown to be primarily dependent on the total calcium content, leading to a higher carbonation degree (~80%) and carbonate content (~70 wt%) for the CEM-I compared to CEM-III samples.

A higher decalcification degree was, however, obtained for the CEM-III samples (Ca/Si ≅ 0.57–0.84) compared to the CEM-I samples (Ca/Si ≅ 0.57–0.96), which is ascribed to the increase in porosity of the sample due to the decalcification. The porosity was further shown to be related to the carbonation degree, where a higher carbonation degree results in a stronger increase in porosity due to shrinkage of the (calcium)-silicate gel.

For both materials, the AC in 0.1 M NaOH was the most efficient carbonation method in terms of carbonation, and decalcification degree. This is hypothesized to be due to the incorporation of sodium during the decalcification of the C–S–H, which initially promotes fast carbonation, but slows the carbonation down due to the formation of a diffusion barrier. In line with the high carbonation degree, the AC_{Na} samples had the highest increase in porosity. Although an increased carbonation degree and higher porosity were achieved for the AC_{Na} samples, the total heat release was slightly lower than expected. This is hypothesized to be due to the sodium in the silicate gel, but further research is required to confirm this.

The overall low carbonation degree of the DC samples was shown to be due to the formation of a carbonate layer around the particles, which limited the calcium diffusion. This layer was further shown to hinder the pozzolanic reactivity and required milling to expose the amorphous silicate phase underneath the carbonate shell.

Calorimetric testing shows that the amount of available silica is the predominant factor affecting the total heat release, where the CEM-III materials had a higher heat release (~89-129 J/g) compared to the CEM-I materials (~61–105 J/g) and the AC samples had a higher heat release compared to the DC samples.

The concept of carbonation efficiency is thus open for interpretation and depends on the envisioned application. The presented work provides a complete picture of how material composition and carbonation method impact the properties of the carbonated material and could therefore be to further optimize carbonation in an industrial context.

CRediT authorship contribution statement

I.E. Teune: Conceptualization, Methodology; Validation; Formal Analysis; Investigation; Writing- Original Draft; Writing – Review & Editing; Visualization.

K. Schollbach: Resources; Supervision; Visualization; Writing – Review & Editing.

M. Florea: Resources; Supervision; Writing – Review & Editing.

H.J.H. Brouwers: Project Administration; Resources, Supervision; Writing – Review & Editing.

Declaration of competing interest

The authors declare that they have no known competing financial interests or personal relationships that could have appeared to influence the work reported in this paper.

Data availability

Data will be made available on request.

Appendix A. Supplementary data

Supplementary data to this article can be found online at https://doi.org/10.1016/j.jobe.2023.107785.

References

[1] H. Lee, K. Calvin, D. Dasgupta, K. Gerhard, Clim. Change 2023 (2023).
[2] I.H. Shah, S.A. Miller, D. Jiang, R.J. Myers, Cement substitution with secondary materials can reduce annual global CO2 emissions by up to 1.3 gigatons, Nat. Commun. 13 (2022) 5758, https://doi.org/10.1038/s41467-022-33289-7.
[3] J. Skocek, M. Zajac, M. Ben Haha, Carbon Capture and Utilization by mineralization of cement pastes derived from recycled concrete, Sci. Rep. 10 (2020) 5614, https://doi.org/10.1038/s41598-020-62503-z.
[4] A. Carriço, J.A. Bogas, M. Guedes, Thermoactivated cementitious materials – a review, Construct. Build. Mater. 250 (2020), 118873, https://doi.org/10.1016/j.conbuildmat.2020.118873.
[5] Z. Shui, D. Xuan, H. Wan, B. Cao, Rehydration reactivity of recycled mortar from concrete waste experienced to thermal treatment, Construct. Build. Mater. 22 (2008) 1723–1729, https://doi.org/10.1016/j.conbuildmat.2007.05.012.
[6] M.V.A. Florea, Z. Ning, H.J.H. Brouwers, Activation of liberated concrete fines and their application in mortars, Construct. Build. Mater. 50 (2014) 1–12, https://doi.org/10.1016/j.conbuildmat.2013.09.012.
[7] S. Goyal, D. Sharma, CO2 sequestration on cement, in: Start-Up Creat, second ed., Elsevier, 2020, pp. 109–142, https://doi.org/10.1016/B978-0-12-819946-6.00006-0.
[8] X. Fang, D. Xuan, B. Zhan, W. Li, C.S. Poon, A novel upcycling technique of recycled cement paste powder by a two-step carbonation process, J. Clean. Prod. 290 (2021), 125192, https://doi.org/10.1016/j.jclepro.2020.125192.
[9] Y.X. Chen, Y. Hendrix, K. Schollbach, H.J. Brouwers, A silica aerogel synthesized from olivine and its application as a photocatalytic support, Construct. Build. Mater. 248 (2020), 118709, https://doi.org/10.1016/j.conbuildmat.2020.118709.
[10] P.C. Hewlett, M. Liska, Lea's Chemistry of Cement and Concrete, 5th Edit, Mathew Deans, Cambridge, 2019.

[11] B.J. Zhan, D.X. Xuan, C.S. Poon, K.L. Scrivener, Characterization of interfacial transition zone in concrete prepared with carbonated modeled recycled concrete aggregates, Cement Concr. Res. 136 (2020), 106175, https://doi.org/10.1016/j.cemconres.2020.106175.
[12] M. Zajac, J. Skocek, P. Durdzinski, F. Bullerjahn, J. Skibsted, M. Ben Haha, Effect of carbonated cement paste on composite cement hydration and performance, Cement Concr. Res. 134 (2020), 106090, https://doi.org/10.1016/j.cemconres.2020.106090.
[13] K. Scrivener, F. Martirena, S. Bishnoi, S. Maity, Calcined clay limestone cements (LC3), Cement Concr. Res. 114 (2018) 49–56, https://doi.org/10.1016/j.cemconres.2017.08.017.
[14] P.P.P. Li, H.J.H.J.H. Brouwers, W. Chen, Q. Yu, Optimization and characterization of high-volume limestone powder in sustainable ultra-high performance concrete, Construct. Build. Mater. 242 (2020), 118112, https://doi.org/10.1016/j.conbuildmat.2020.118112.
[15] R. Aylard, L. Hawson, Cement Sustainability Initiative, Conches-Geneva, 2002.
[16] J. Lehne, F. Preston, Making Concrete Change; Innovation in Low-Carbon Cement and Concrete, 2018. London, www.chathamhouse.org.
[17] R.M. Andrew, Global CO2 emissions from cement production, 1928–2018, Earth Syst. Sci. Data 11 (2019) 1675–1710, https://doi.org/10.5194/essd-11-1675-2019.
[18] S. Steiner, B. Lothenbach, T. Proske, A. Borgschulte, F. Winnefeld, Effect of relative humidity on the carbonation rate of portlandite, calcium silicate hydrates and ettringite, Cement Concr. Res. 135 (2020), 106116, https://doi.org/10.1016/j.cemconres.2020.106116.
[19] M. Zajac, J. Skibsted, F. Bullerjahn, J. Skocek, Semi-dry carbonation of recycled concrete paste, J. CO2 Util. 63 (2022), https://doi.org/10.1016/j.jcou.2022.102111.
[20] R. Hay, J. Li, K. Celik, Phase evolution, micromechanical properties, and morphology of calcium (alumino)silicate hydrates C-(A-)S-H under carbonation, Cement Concr. Res. 152 (2022), 106683, https://doi.org/10.1016/j.cemconres.2021.106683.
[21] T.F. Sevelsted, J. Skibsted, Carbonation of C-S-H and C-A-S-H samples studied by 13C, 27Al and 29Si MAS NMR spectroscopy, Cement Concr. Res. 71 (2015) 56–65, https://doi.org/10.1016/j.cemconres.2015.01.019.
[22] V. Shah, K. Scrivener, B. Bhattacharjee, S. Bishnoi, Changes in microstructure characteristics of cement paste on carbonation, Cement Concr. Res. 109 (2018) 184–197, https://doi.org/10.1016/j.cemconres.2018.04.016.
[23] E. Kangni-Foli, S. Poyet, P. Le Bescop, T. Charpentier, F. Bernachy-Barbé, A. Dauzères, E. L'Hôpital, J.-B. d'Espinose de Lacaillerie, Carbonation of model cement pastes: the mineralogical origin of microstructural changes and shrinkage, Cement Concr. Res. 144 (2021), 106446, https://doi.org/10.1016/j.cemconres.2021.106446.
[24] B. Šavija, M. Luković, Carbonation of cement paste: understanding, challenges, and opportunities, Construct. Build. Mater. 117 (2016) 285–301, https://doi.org/10.1016/j.conbuildmat.2016.04.138.
[25] M. Zajac, J. Skibsted, P. Durdzinski, F. Bullerjahn, J. Skocek, M. Ben Haha, Kinetics of enforced carbonation of cement paste, Cement Concr. Res. 131 (2020), 106013, https://doi.org/10.1016/j.cemconres.2020.106013.
[26] M. Zajac, J. Skibsted, M. Ben Haha, Effect of alkalis on enforced carbonation of cement paste: mechanism of reaction, J. Am. Ceram. Soc. 104 (2021) 1076–1087, https://doi.org/10.1111/jace.17481.
[27] M. Zajac, J. Skibsted, J. Skocek, P. Durdzinski, F. Bullerjahn, M. Ben Haha, Phase assemblage and microstructure of cement paste subjected to enforced, wet carbonation, Cement Concr. Res. 130 (2020), 105990, https://doi.org/10.1016/j.cemconres.2020.105990.
[28] M. Zajac, J. Skibsted, P. Durdzinski, M. Ben Haha, Effect of alkalis on products of enforced carbonation of cement paste, Construct. Build. Mater. 291 (2021), 123203, https://doi.org/10.1016/j.conbuildmat.2021.123203.
[29] C. Xavier, C. Oliveira, Decarbonisation Options for the Dutch Cement Industry, 2021. The Hague.
[30] EN 196-3 Method of Testing Cement – Part 3: Determination of Setting Times and Soundness, 2016.
[31] C. van Hoek, J. Small, S. van der Laan, Large-area phase mapping using P h A se R ecognition and C haracterization (PARC) software, micros, Today Off. 24 (2016) 12–21, https://doi.org/10.1017/S1551929516000572.
[32] K. Scrivener, R. Snellings, B. Lothenbach, A Practical Guide to Microstructural Analysis of Cementitious Materials, CRC Press Taylor & Francis Group, Boca Raton, FL, 2016.
[33] F. Avet, R. Snellings, A. Alujas Diaz, M. Ben Haha, K. Scrivener, Development of a new rapid, relevant and reliable (R3) test method to evaluate the pozzolanic reactivity of calcined kaolinitic clays, Cement Concr. Res. 85 (2016) 1–11, https://doi.org/10.1016/j.cemconres.2016.02.015.
[34] P. Shen, Y. Jiang, Y. Zhang, S. Liu, D. Xuan, J. Lu, S. Zhang, C.S. Poon, Production of aragonite whiskers by carbonation of fine recycled concrete wastes: an alternative pathway for efficient CO2 sequestration, Renew. Sustain. Energy Rev. 173 (2023), 113079, https://doi.org/10.1016/j.rser.2022.113079.
[35] S. Goto, S. Kenzo, K. Takeshi, Calcium silicate products, J. Am. Ceram. Soc. 78 (1995) 2867–2872.
[36] J.J. Chen, J.J. Thomas, H.F.W. Taylor, H.M. Jennings, Solubility and structure of calcium silicate hydrate, Cement Concr. Res. 34 (2004) 1499–1519, https://doi.org/10.1016/j.cemconres.2004.04.034.
[37] M. Yoo, S.J. Han, J.H. Wee, Carbon dioxide capture capacity of sodium hydroxide aqueous solution, J. Environ. Manag. 114 (2013) 512–519, https://doi.org/10.1016/j.jenvman.2012.10.061.
[38] S.Y. Yang, Y. Yan, B. Lothenbach, J. Skibsted, Incorporation of sodium and aluminum in cementitious calcium-alumino-silicate-hydrate C-(A)-S-H phases studied by 23Na, 27Al, and 29Si MAS NMR spectroscopy, J. Phys. Chem. C 125 (2021) 27975–27995, https://doi.org/10.1021/acs.jpcc.1c08419.
[39] E. Bernard, Y. Yan, B. Lothenbach, Effective cation exchange capacity of calcium silicate hydrates (C-S-H), Cement Concr. Res. 143 (2021), 106393, https://doi.org/10.1016/j.cemconres.2021.106393.
[40] P. Bots, L.G. Benning, J.D. Rodriguez-Blanco, T. Roncal-Herrero, S. Shaw, Mechanistic insights into the crystallization of amorphous calcium carbonate (ACC), Cryst, Growth Des 12 (2012) 3806–3814, https://doi.org/10.1021/cg300676b.
[41] J.J. Chen, J.J. Thomas, H.M. Jennings, Decalcification shrinkage of cement paste, Cement Concr. Res. 36 (2006) 801–809, https://doi.org/10.1016/j.cemconres.2005.11.003.
[42] L. Fernández-Carrasco, D. Torrens-Martín, L.M. Morales, S. Martínez-Ramírez, Infrared spectroscopy in the analysis of building and construction materials, in: Infrared Spectrosc. - Mater. Sci. Eng. Technol, 2012, https://doi.org/10.5772/36186.
[43] N.V. Vagenas, A. Gatsouli, C.G. Kontoyannis, Quantitative analysis of synthetic calcium carbonate polymorphs using FT-IR spectroscopy, Talanta 59 (2003) 831–836, https://doi.org/10.1016/S0039-9140(02)00638-0.
[44] T. Mayerhöfer, Wave Optics in Infrared Spectroscopy, 2021, https://doi.org/10.13140/RG.2.2.14293.55520.
[45] B. Udvardi, I.J. Kovács, T. Fancsik, P. Kónya, M. Bátori, F. Stercel, G. Falus, Z. Szalai, Effects of particle size on the attenuated total reflection spectrum of minerals, Appl. Spectrosc. 71 (2017) 1157–1168, https://doi.org/10.1177/0003702816670914.
[46] E. John, D. Stephan, Calcium silicate hydrate—in-situ development of the silicate structure followed by infrared spectroscopy, J. Am. Ceram. Soc. (2021) 1–14, https://doi.org/10.1111/jace.18019.
[47] R. Maddalena, C. Hall, A. Hamilton, Effect of silica particle size on the formation of calcium silicate hydrate [C-S-H] using thermal analysis, Thermochim. Acta 672 (2019) 142–149, https://doi.org/10.1016/j.tca.2018.09.003.
[48] M. Zajac, G. Bolte, J. Skocek, M. Ben Haha, Modelling the effect of the cement components fineness on performance and environmental impact of composite cements, Construct. Build. Mater. 276 (2021), 122108, https://doi.org/10.1016/j.conbuildmat.2020.122108.
[49] A. Ouzia, K. Scrivener, The needle model: a new model for the main hydration peak of alite, Cement Concr. Res. 115 (2019) 339–360, https://doi.org/10.1016/j.cemconres.2018.08.005.
[50] E. Berodier, K. Scrivener, Understanding the filler effect on the nucleation and growth of C-S-H, J. Am. Ceram. Soc. 97 (2014) 3764–3773, https://doi.org/10.1111/jace.13177.
[51] S.P. Veetil, M. Hitch, Recent developments and challenges of aqueous mineral carbonation: a review, Int. J. Environ. Sci. Technol. 17 (2020) 4359–4380, https://doi.org/10.1007/s13762-020-02776-z.
[52] Y.S. Han, G. Hadiko, M. Fuji, M. Takahashi, Effect of flow rate and CO2 content on the phase and morphology of CaCO3 prepared by bubbling method, J. Cryst. Growth 276 (2005) 541–548, https://doi.org/10.1016/j.jcrysgro.2004.11.408.